



1 **A muographic study of a scoria cone from 11**
2 **directions using nuclear emulsion cloud chambers**

3

4 Seigo Miyamoto¹, Shogo Nagahara^{1,2}, Kunihiro Morishima³, Toshiyuki Nakano³,
5 Masato Koyama⁴, Yusuke Suzuki⁵

6

7 ¹Earthquake Research Institute, The University of Tokyo, 1-1-1 Yayoi, Bunkyo-ku,
8 Tokyo, 113-0032, Japan.

9 ²Graduate School of Human Development and Environment, Kobe University, 3-11
10 Tsurukabuto, Nada-ku, Kobe, Hyogo, 657-8501, Japan.

11 ³Fundamental Particle Physics Laboratory, Graduate School of Science of Nagoya
12 University, Furocho, Chikusa-ku, Nagoya, Aichi, 464-8602, Japan.

13 ⁴Department of Education, Shizuoka University, 836 Ohya, Suruga-ku, Shizuoka City,
14 Shizuoka, Japan.

15 ⁵STORY, Ltd., 2-2-5-2321, Minatomachi, Naniwa-ku, Osaka City, Osaka, Japan.

16 *Correspondence to:* Seigo Miyamoto (miyamoto@eri.u-tokyo.ac.jp)



17 **Abstract**

18 One of the key challenges for muographic studies is to reveal the detailed 3D density
19 structure of a volcano by increasing the number of observation directions. 3D density
20 imaging by multi-directional muography requires that the individual differences in the
21 performance of the installed muon detectors are small and that the results from each
22 detector can be derived without any bias in the data analysis. Here we describe a pilot
23 muographic study of the Izu–Omuroyama scoria cone in Shizuoka Prefecture, Japan,
24 from 11 directions, using a new nuclear emulsion detector design optimized for quick
25 installation in the field. We describe the details of the data analysis and present a
26 validation of the results.

27 The Izu–Omuroyama scoria cone is an ideal target for the first multi-directional
28 muographic study, given its expected internal density structure and the topography
29 around the cone. We optimized the design of the nuclear emulsion detector for rapid
30 installation at multiple observation sites in the field, and installed these at 11 sites
31 around the volcano. The images in the developed emulsion films were digitized into
32 segmented tracks with a high-speed automated readout system. The muon tracks in
33 each emulsion detector were then reconstructed. After the track selection, including
34 straightness filtering, the detection efficiency of the muons was estimated. Finally, the
35 density distributions in 2D angular space were derived for each observation site by
36 using a muon flux and attenuation models.

37 The observed muon flux was compared with the expected value in the free sky, and is
38 $88\% \pm 4\%$ in the forward direction and $92\% \pm 2\%$ in the backward direction. The
39 density values were validated by comparison with the values obtained from gravity
40 measurements, and are broadly consistent, except for one site. The excess density at



41 this one site may indicate that the density inside the cone is non-axisymmetric, which
42 is consistent with a previous geological study.

43 **1 Introduction**

44 Scoria or cinder cones are a simple volcanic structure, along with stratovolcanoes,
45 shield volcanoes, and lava domes. Understanding the internal structure of scoria cones
46 is important for volcanic hazard assessments. The internal structure of scoria cones
47 has been mainly investigated by geological approaches. Kereszturi and Németh (2012)
48 presented a schematic cross-section of typical scoria cones, and Geshi and Neri (2014)
49 presented detailed photographs of the feeder dike and interior of a scoria cone formed
50 by the 1809 Etna eruption. Yamamoto (2003) investigated outcrops of the interior of
51 scoria cones in the Ojika-jima monogenetic volcano group, Nagasaki Prefecture, Japan.
52 Yamamoto (2003) classified 40 scoria cones according to their degree of interior welding
53 and proposed a link between lava outflow and cone collapse. However, scoria cones with
54 such outcrops are rare, and the internal structure can vary markedly among cones.
55 Therefore, non-destructive methods are required to investigate scoria cones that lack
56 outcrops.

57 Muography is a non-destructive technique for investigating the internal density
58 structure of large objects, employing the strong penetrating force of muons, which are
59 high-energy elementary particles contained in cosmic rays. Muography has also been
60 used for studying volcanoes, including visualization of a shallow conduit (e.g., Tanaka
61 et al., 2009), detection of temporal changes in water level due to hydrothermal activity
62 (Jourde et al., 2016), and 3D density imaging of a lava dome using a joint inversion of
63 muographic and gravity data (Nishiyama et al., 2017).



64 In unidirectional muography, the only measurable quantity is the density length,
65 which is the integral of density and length along the muon direction. It has no spatial
66 resolution along the muon path. Therefore, even if an interesting density contrast is
67 found below the crater, this could reflect contributions from other parts of the volcanic
68 body. Similar to X-ray computed tomography, which has been developed as a 3D density
69 imaging technique, muography can obtain 3D spatial resolution by increasing the
70 number of observation directions. In previous studies, muography of volcanoes has
71 been conducted in two or three directions (Tanaka et al., 2010; Rosas-Carbajal et al.,
72 2017). However, the spatial resolution is not sufficient to determine the detailed
73 structure of the volcanic interior. Nagahara and Miyamoto (2018) undertook a 3D
74 density reconstruction based on multi-directional muography and the filtered back-
75 projection technique. Their study showed that it is necessary to increase the number of
76 directions to obtain 3D spatial resolution in volcanological studies.

77 Nuclear emulsion is a type of muon detector, and has been used for studies of
78 volcanoes (Tanaka et al., 2007; Nishiyama et al., 2014; Tioukov et al., 2019). The
79 trajectories of high-energy charged particles that pass through an emulsion film are
80 recorded as aligned silver grains with micron-scale resolution (Nakamura et al., 2005;
81 Tioukov et al., 2019; Nishio et al., 2020). The positions and slopes of aligned grains in a
82 developed emulsion film are digitized with an automated emulsion readout system
83 (Kreslo et al., 2008; Morishima and Nakano, 2010; Bozza et al., 2012; Yoshimoto et al.,
84 2017). Unlike hodoscopes using scintillator bars (e.g., Saracino et al., 2017) or multi-
85 wire proportional chambers (Olah et al., 2018), a nuclear emulsion film does not have
86 temporal resolution. In contrast, an emulsion detector does not require electricity,



87 which facilitates the installation of such detectors around volcanoes where the
88 infrastructure is not well developed.

89 In muographic studies of a volcano, contamination by low-momentum particles must
90 be removed to derive the correct density (Nishiyama et al., 2014, 2016). Thus, nuclear
91 emulsion detectors have often been used as an emulsion cloud chamber (ECC), which
92 comprises alternating layers of films and lead or iron plates (e.g., Kodama et al., 2003).
93 An ECC detector can measure the momentum of the charged particle by detecting
94 deflection angles caused by multiple Coulomb scattering (Agafonova et al., 2012). For
95 multiple Coulomb scattering, there is a relationship between the maximum detectable
96 momentum p_{max} and position resolution y_{reso} as follows:

$$97 \quad p_{max} \sim \alpha X_0^{-0.5} x^{1.5} y_{reso}^{-1} \quad (1)$$

98 where α is a constant, X_0 is the radiation length of a material, and x is the thickness of
99 the material. The position resolution of the newest scintillator hodoscope or MWPC is
100 on the order of 1 mm (Saracino et al., 2017; Olah et al., 2018). In the case of nuclear
101 emulsion, the resolution is about 1 μm . When using ECC, the thickness of the material
102 can be reduced to 1/100 while maintaining the same p_{max} , which is advantageous in
103 terms of transportation in the field.

104 A new design of the ECC detector was also required for its rapid installation at
105 multiple observation sites in the field. In a previous study of volcano observations
106 using the ECC detector (Nishiyama et al., 2014), rapid installation of the detector was
107 not required because the number of observation sites was just one. It is also important
108 to establish a data analysis procedure for the muon tracks recorded by the ECC
109 detectors. To derive an accurate density value for the volcanic body, it is necessary to
110 remove low-momentum contamination, estimate the detection efficiency, and validate



111 the results. In addition, for bias-free 3D imaging by multi-directional muography, the
112 installed muon detectors must show similar performance.

113 **2 Izu–Omuroyama scoria cone**

114 The Izu–Omuroyama scoria cone (34°54′11″N, 139°05′40″E; 580 m a.s.l.) is one of the
115 largest scoria cones in the world, and is part of the Higashi Izu monogenetic volcano
116 group (Aramaki and Hamuro, 1977), which is located in the northeastern Izu
117 Peninsula, Ito City, Shizuoka Prefecture, Japan. It is considered to have formed at 4
118 ka, based on ¹⁴C dating (Saito et al., 2003). The basal diameter is 1,000 m, the height is
119 280 m from the base, and the typical slope of its flanks are 29–32°. The center of the
120 cone contains a crater that is 250 m wide and 40 m deep. The volume of the cone is
121 $71 \times 10^6 \text{ m}^3$, and lava with a volume of $\sim 10^8 \text{ m}^3$ has flowed out from the base of the
122 cone (Koyano et al., 1996). The lava is a basaltic andesite with 54–56 wt.% SiO₂
123 (Hamuro, 1985).

124 Although the shape of the Izu–Omuroyama scoria cone appears to be axisymmetric
125 (Fig. 1), a geological study suggested it has an anisotropic structure due to the
126 following reasons. (i) During/after the growth of the cone, some interior parts became
127 welded due to loading, residual heat, and a low cooling rate. As a result, some denser
128 material formed. (ii) At the end of the eruption, a lava lake was formed in the crater,
129 and the lava flowed out to the western foot of the cone. (iii) There is a small crater on
130 the south side of the cone, which is thought to have formed when the main crater was
131 blocked at the end of the eruption (Koyano et al., 1996).

132 The bulk density of typical continental crust is about $2.6\text{--}2.7 \times 10^3 \text{ kg m}^{-3}$. The bulk
133 densities reported for scoria deposits are $0.84\text{--}1.01 \times 10^3 \text{ kg m}^{-3}$ (Taha and Mohamed,



134 2013) and $0.56\text{--}1.20 \times 10^3 \text{ kg m}^{-3}$ (Bush, 2001). Therefore, the maximum expected
135 density contrast is about $1.4\text{--}2.0 \times 10^3 \text{ kg m}^{-3}$, due to the difference in porosity
136 between welded rocks and scoria deposits. In addition, the Izu–Omuroyama scoria cone
137 is an ideal target for multi-directional muography due to the accessibility to detector
138 sites and absence of muographic shadows from any direction caused by other
139 topographic features.
140



141 Figure 1. Photograph of the Izu–Omuroyama scoria cone from the northwest, taken by
142 an unmanned aerial vehicle (Koyama, 2017).
143



144 **3 Multi-directional muography observations using emulsion cloud chambers**

145 **3.1 Detector design**

146 Emulsion films were manufactured by pouring 70 μm of nuclear emulsion on both
147 sides of a 180 μm -thick plastic base. The size of a film is 125 \times 100 mm. The films were
148 vacuum-packed in a light-blocking envelope to maintain their planar form, which
149 prevented air bubbles forming between the envelope and film, and made it easy to
150 handle the films in the field.

151 The detector used for the 2018 observations is basically the same as that of Nishiyama
152 et al. (2014), and only the number of lead plates was different. The former consists of
153 20 films and 9 plates of 1-mm-thick lead, the latter consists of 20 films and 19 lead
154 plates. At the time of installation in 2018, the films, lead plates, and supports were all
155 in pieces and, therefore, a lot of time and effort was required for assembly in the field.
156 The more efficient detector design was required for rapid and error-free installation.

157 The detector used in the 2019 observations was improved. It consists of an ECC and
158 an outer box. The ECC consists of 20 emulsion films and 19 lead plates, each 1 mm
159 thick (Fig. 2a). An aluminum frame was fixed to a lead plate with a thin sheet of glue,
160 and then an emulsion film with the light-blocking envelope was attached with scotch
161 tape. In this paper, we term this unit the emulsion–lead plate (EL plate; Fig. 2a). The
162 EL plate was designed for quick assembly in the field.

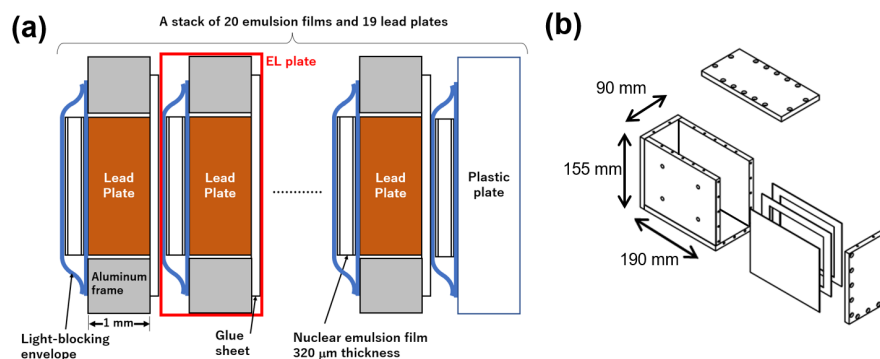
163 The outer box consists of 10-mm-thick aluminum plates (Fig. 2b). The outer size of
164 this box is 190 mm in width, 155 mm in height, and 90 mm in depth. An ECC and
165 strong springs were placed in the box. There are four screw holes on one side of the box,
166 and by turning the bolts and pushing the spring plate, a uniform pressure ($\sim 10^5$ Pa)



167 was applied to the ECC. This pressure prevents the film from stretching and shrinking
168 due to temperature changes.

169 Given that there is no temporal resolution in emulsion films, we needed to add time
170 information to the ECC. In previous muographic studies using emulsion films,
171 researchers have used emulsion films with a different alignment during the muon
172 observations and standby (e.g., Tanaka et al., 2007). In the present study, the corners of
173 the EL plates were aligned during the muon observations, while the corners were
174 intentionally shifted a few millimeters horizontally and fixed with clamps during
175 standby (Fig. 3). This alignment difference distinguishes passing charged particles
176 during non-observation and observation periods by pattern matching of each emulsion
177 film. By using this procedure, the time to set the alignment between each EL plate in
178 the field is <30 s. Although the muon tracks that pass through an ECC during the
179 alignment set-up may become noise, our procedure reduced such tracks.

180



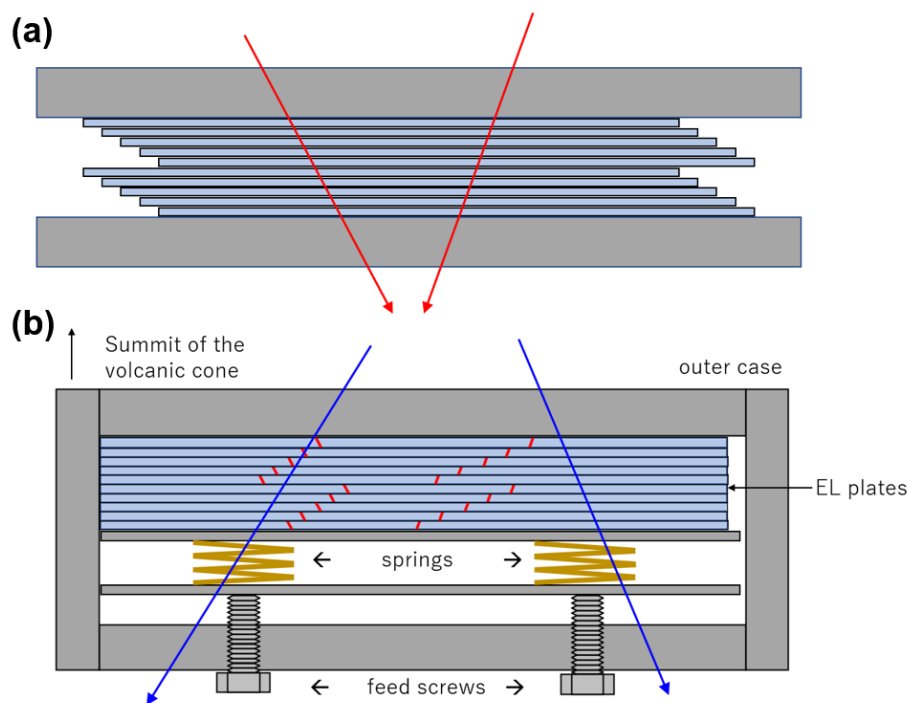
181

182 Figure 2. Design of the ECC and outer box. (a) Schematic cross-section of the EL plates
183 and an ECC. The EL plate consists of a 1-mm-thick aluminum frame, 1-mm-thick lead
184 plate, 100-μm-thick glue sheet that fixes a lead plate to an aluminum frame, and an
185 emulsion film with a light-blocking envelope. An ECC consists of 19 EL plates and an
186 emulsion film with a plastic plate. (b) Schematic of the aluminum outer box. The
187 thickness of the aluminum plate is 10 mm. The ECC shown in (a) was set inside this
188 box. There are four holes for feed screws in the front plate.

189



190



191

192

193 Figure 3. (a) View of the EL plates from above during standby. The EL plates were
194 intentionally shifted a few millimeters horizontally and fixed with a pair of steel plates
195 and clamp. The red lines represent the muon tracks in this alignment. (b) View from
196 above during the observations. The EL plates were aligned to the side of the outer box,
197 and fixed by the springs and feed screws. The blue lines represent muon tracks during
198 observations. Note that the red tracks cannot be reconstructed in this alignment.

199

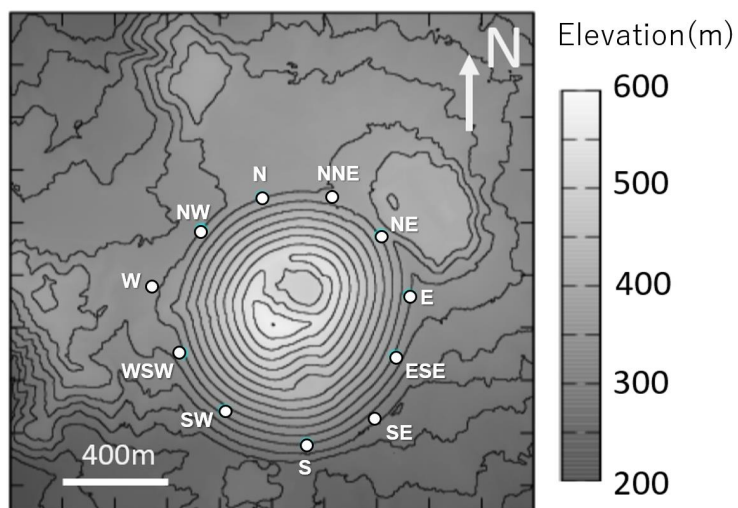


200 **3.2 Installation**

201 The detectors were installed at three sites in 2018 and eight sites in 2019 around the
202 Izu–Omuroyama scoria cone (Fig. 4; Table 1). Each detector was buried in a hole that
203 was about 40 cm deep to avoid high temperatures due to direct sunlight. This is done
204 because the number of latent image specks decreases, and the number of randomly
205 generated specks increases, under high-temperature conditions (Nishio et al., 2020).
206



207



208

209

210 Figure 4. Topography of the Izu–Omuroyama scoria cone. White dots represent
211 observation sites.

212

Detector site ID	Effective area (cm ²)	Exposure time (days)
W, SE, and NNE (2018)	120	60
N, NW, WSW, SW, S, ESE, E, and NE (2019)	240	90

213 Table 1. Effective area and muon exposure time for each detector.

214



215

216 The installation procedure at each observation site in 2019 was as follows (Fig. 5).

- 217 1) Carry the outer box and EL plates to the observation site.
- 218 2) Measure the coordinates of the site with a hand-held GPS (GERMIN; model GPS
219 eTrex 30J). The typical uncertainty of the latitudinal and longitudinal coordinates
220 is 3 m.
- 221 3) Dig a hole in the ground with horizontal dimensions of 60×40 cm and a depth of
222 40 cm.
- 223 4) Flatten the base of the hole, place a plastic bag inside the hole, and lay down a
224 piece of plywood.
- 225 5) Put double-sided tape on the bottom of the outer box and place it on the plywood.
- 226 6) Put the stack of EL plates into the box and quickly align these (<30 s).
- 227 7) Close the cap of the outer box.
- 228 8) Turn the feed screws to increase the pressure.
- 229 9) Measure the attitude of the outer box (i.e., the yaw [azimuth], roll, and pitch) with
230 a fiber optic gyro (Japan Aviation Electronics Industry Ltd.; model FOG JM7711;
231 Watanabe et al., 2000) and digital leveler. The typical errors on the yaw, roll, and
232 pitch are 8.7×10^{-3} , 1.0×10^{-3} , and 1.0×10^{-3} , respectively.
- 233 10) Cover with styrofoam to avoid heating from the ground surface.
- 234 11) Close the plastic bag to keep water out.
- 235 12) Backfill the hole.

236

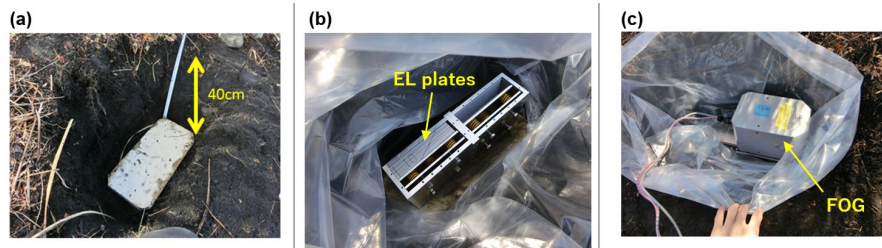
237 The time taken for this installation was ~ 2 h for each site, and we installed detectors
238 as three sites in a day in 2019. The detector retrieval procedure was the opposite of the



239 installation procedure. The 380 films were developed in a darkroom. The deposited
240 silver particles on the surface of the films were removed with anhydrous ethanol. The
241 gelatin of the sensitive layer was swollen with a glycerin solution to obtain the
242 optimum thickness for an automated track readout system, which is described in the
243 next section.
244



245



246

247

248 Figure 5. Photographs showing the installation procedure. (a) Dig a hole and place a
249 plywood sheet in the bottom. (b) Place the outer box in the hole and put a stack of EL
250 plates into the box. The plates were aligned over a period of <30 s. After closing the top
251 plate of the box, the feed screws were tightened to increase the pressure. (c) The yaw,
252 roll, and pitch were measured with a fiber optic gyro (FOG) and digital leveler.

253



254 **4 Track reconstruction, selection, and detection efficiency estimation**

255 **4.1 Track reconstruction**

256 A track of a high-energy charged particle is recorded as an aligned line of silver grains
257 in the emulsion film (e.g., Nakamura et al., 2005). The images in the 380 nuclear
258 emulsion films were scanned and the positions and slopes of the tracks were digitized
259 by “HTS”, which is a high-speed automated track readout system at Nagoya University
260 (Yoshimoto et al., 2017). For each ECC, the tracks of the charged particles were
261 digitally reconstructed from the segmented tracks in 20 films. NETSCAN 2.0 software
262 was used for track reconstruction (Hamada et al., 2012). NETSCAN 2.0 rapidly
263 corrects for film distortions and local misalignments between films by using many
264 tracks recorded over a large area. It then outputs all possible connections as the final
265 result. NETSCAN 2.0 has been used in various fields, such as neutrino physics
266 (Hiramoto et al., 2020), cosmic ray astronomy (Takahashi et al., 2015), and muographic
267 studies of Egyptian pyramids (Morishima et al., 2017). The typical procedure for the
268 track reconstruction is as follows.

269

- 270 1) Reconstruct the “base track”, which is connected between the emulsion layers
271 across the plastic base of 170 μm in a film.
- 272 2) Reconstruction of the “linklet”, which is the base track pair between adjacent films
273 across lead plates.
- 274 3) Reconstruction of the tracks that connect across the whole ECC. If no base track
275 was found in two consecutive films on the extension of a track, then the track was
276 considered to have stopped.



277

278 For example, in ECC_ID = 02, 8.9×10^6 base tracks, 3.2×10^6 linklets in a pair of
279 adjacent films, and 1.7×10^7 tracks in an entire ECC were reconstructed.

280 4.2 Track selection

281 NETSCAN 2.0 outputs all possible track connections. Therefore, it is necessary to
282 carefully select the tracks for the muographic analysis. A schematic example of the
283 output tracks is shown in Fig. 6. Most of the branches can be considered to represent
284 contamination by fake base tracks caused by random noise, or the coincidental
285 occurrence of low-energy positrons/electrons on parallel slopes in the vicinity of the real
286 tracks (e.g., Fig. 6; cases 2 and 3). Some branches consist of a pair of straight tracks
287 with small closest distances and similar angles (Fig. 6; case 4). In this case, the two
288 tracks should be separated.

289 The following χ^2/ndf value was calculated for all tracks for the low momentum cut-
290 off:

$$291 \quad \chi^2/ndf = \sum_m \left[\left(\frac{\Delta\theta_R^m}{\sigma_R^m} \right)^2 + \left(\frac{\Delta\theta_L^m}{\sigma_L^m} \right)^2 \right] / ndf \quad (2)$$

292 where ndf is the number of degrees of freedom and m is the index of adjacent film pairs
293 (i.e., [1,2], [2,3], [3,4], ..., and [18,19], [19,20] in Fig. 6) or with one skip if there was a
294 base track inefficiency (i.e., [1,3], [2,4], [3,5], ..., [17,19], [18,20]). $\Delta\theta_R^m =$
295 $(\Delta\theta_x^m \times \tan \theta_x + \Delta\theta_y^m \times \tan \theta_y) / \sqrt{\tan^2 \theta_x + \tan^2 \theta_y}$ and $\Delta\theta_L^m = (\Delta\theta_y^m \times \tan \theta_x -$
296 $\Delta\theta_x^m \times \tan \theta_y) / \sqrt{\tan^2 \theta_x + \tan^2 \theta_y}$, and $\Delta\theta_x^m$ and $\Delta\theta_y^m$ are angular differences along the
297 x, y coordinates of the ECC. σ_R^m and σ_L^m are the root-mean-square of $\Delta\theta_R^m$ and $\Delta\theta_L^m$,
298 which were calculated for every adjacent film pair in every ECC (Fig. 7). Figure 8



299 shows the distribution of χ^2/ndf for all tracks in an ECC.

300 The procedure for track selection is as follows.

301 1) Select tracks that start from one of the two most upstream (i.e., summit cone side)

302 films and stop at one of the two most downstream films.

303 2) Select tracks with $\chi^2/ndf < 5.0$.

304 3) If a track has any branches, then:

305 a) If the shared proportion of track length is $\geq 20\%$, choose the longest branch. If

306 the track lengths are the same, then choose the branch with the smallest

307 χ^2/ndf .

308 b) If the shared proportion of track length is $< 20\%$ (Fig. 6; case 4), then the

309 branches were divided into two tracks.

310 We estimated the effect of the straightness filtering using $\chi^2/ndf < 5.0$. Figure 9 shows

311 the momentum filtering efficiency. The path length in the lead plates becomes longer

312 when the track has a larger slope, and thus the momentum also becomes higher. Based

313 on the background noise study by Nishiyama et al. (2016), the size of the mountain

314 body used in the simulation and the Izu–Omuroyama scoria cone is broadly the same,

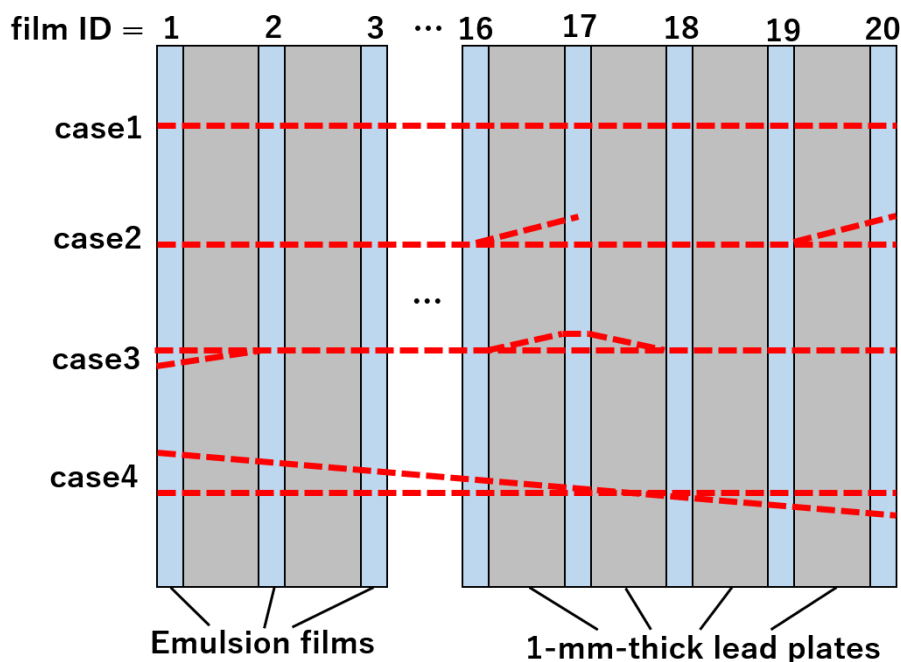
315 and thus the rejection efficiency should be sufficient. For example, after the track

316 selection, 1.7×10^6 tracks were selected at the site “N”.

317



318



319

320

321 Figure 6. Schematic examples of typical reconstructed tracks in an ECC obtained by

322 NETSCAN 2.0. Upstream means towards the volcanic cone side and downstream

323 means the backward free sky direction.

324 Case 1: a straight track without any branches.

325 Case 2: a straight track with a branch in the middle and downstream films. The track

326 branch in the middle was rejected by selection step (1). The branch in the most

327 downstream film was merged into the straight track by selection step 3a.

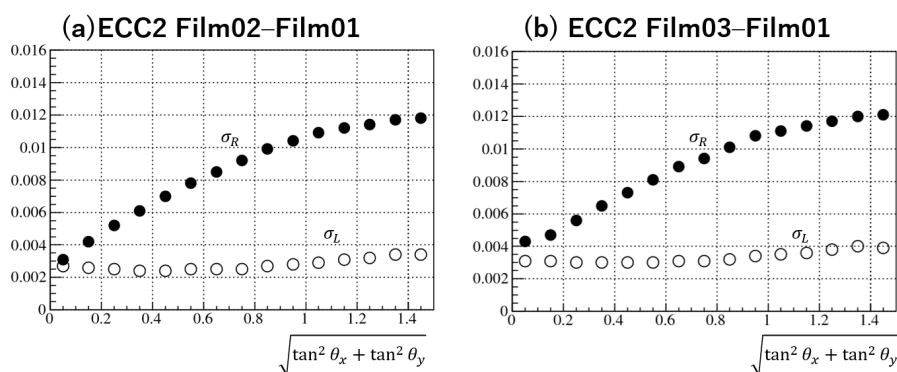
328 Case 3: branches in the upstream and middle films. Both branches were merged into a

329 straight track by selection step 3a.

330 Case 4: a pair of straight tracks with small closest distances and similar angles. If the



331 shared proportion of the track length was <20%, the tracks were divided into two
332 different tracks by selection step 3b.
333

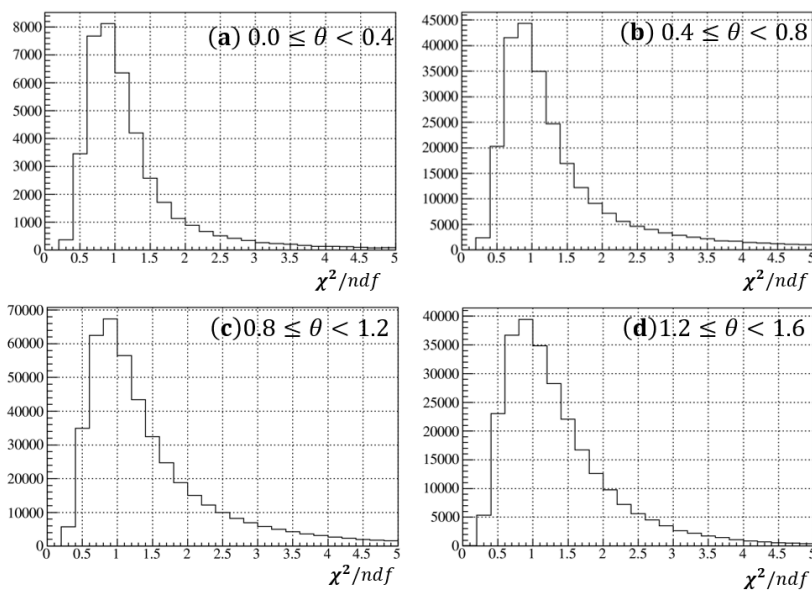


334

335 Figure 7. Examples of σ_R and σ_L as a function of $\sqrt{\tan^2 \theta_x + \tan^2 \theta_y}$. The values were

336 determined by the ECC and used to calculate the value of Eq. (2).

337

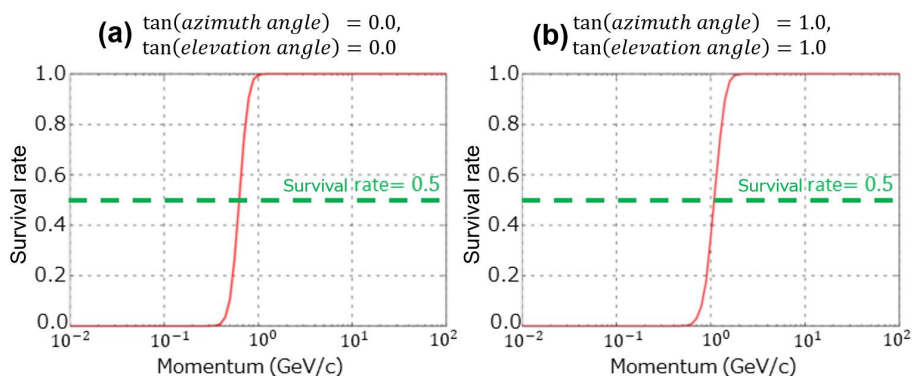


338

339 Figure 8. Example of the χ^2/ndf distribution for selected tracks as a function of $\theta =$

340 $\sqrt{\tan^2 \theta_x + \tan^2 \theta_y}$ in an ECC. (a) $0 \leq \theta < 0.4$, (b) $0.4 \leq \theta < 0.8$, (c) $0.8 \leq \theta < 1.2$, and (d)

341 $1.2 \leq \theta < 1.6$.



342

343 Figure 9. Survival rate of muons after the straightness cut-off as a function of

344 momentum. (a) Track angles with $\tan(\text{relative azimuth}) = 0.0$ and

345 $\tan(\text{elevation angle}) = 0.0$. (b) Track angles with $\tan(\text{relative azimuth}) = 1.0$ and

346 $\tan(\text{elevation angle}) = 1.0$. The path length in the lead plates becomes longer when the

347 track has a larger slope, and thus the remaining momentum also becomes higher for

348 the latter case. The momentum values at a survival rate of 0.5 are 0.6 and 1.1 GeV/c,

349 respectively.

350



351 **4.3 Detection efficiency estimation**

352 The muon detection efficiency can be estimated by investigating the percentage of
353 tracks that have a base track in a film. In this paper, we term this percentage the “fill
354 factor”. The fill factor ε can be defined as follows:

$$355 \quad \varepsilon_j(\theta_x, \theta_y) = \frac{N_j(\theta_x, \theta_y)}{N_{j-1, j+1}(\theta_x, \theta_y)} \quad (3)$$

356 where j is a film ID, $N_{j-1, j+1}(\theta_x, \theta_y)$ is the number of tracks in which base tracks were
357 found in films $j-1$ and $j+1$, and $N_j(\theta_x, \theta_y)$ is the number of tracks in which base
358 tracks were found in films $j-1$, j , and $j+1$. The fill factor depends on the films and
359 track slopes θ_x and θ_y .

360 Using the fill factor $\varepsilon_j(\theta_x, \theta_y)$ and $\bar{\varepsilon}_j(\theta_x, \theta_y) = 1 - \varepsilon_j(\theta_x, \theta_y)$, the muon detection
361 efficiency ϵ in an ECC can be calculated as follows:

$$362 \quad \epsilon(\theta_x, \theta_y) = \sum_{hit\ pattern} \varepsilon_1 \times \bar{\varepsilon}_2 \times \varepsilon_3 \times \dots \times \bar{\varepsilon}_{18} \times \varepsilon_{19} \times \varepsilon_{20} \quad (4)$$

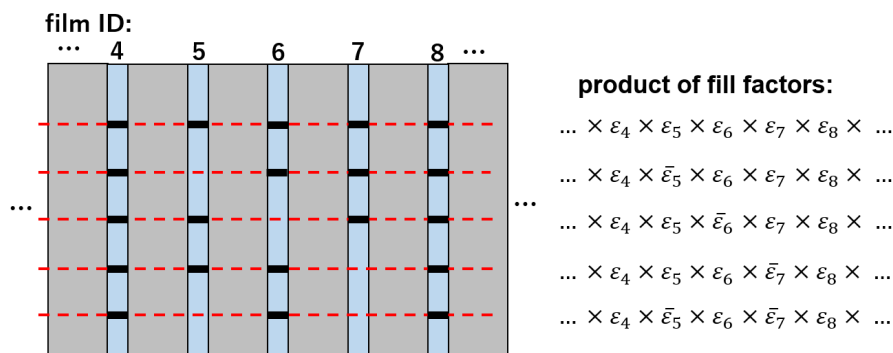
363 where *hit pattern* is the summation for all possible hit patterns (e.g., $\varepsilon_1 \times \bar{\varepsilon}_2 \times \varepsilon_3 \times$
364 $\dots \times \bar{\varepsilon}_{18} \times \varepsilon_{19} \times \varepsilon_{20}$ or $\bar{\varepsilon}_1 \times \varepsilon_2 \times \varepsilon_3 \times \dots \times \varepsilon_{18} \times \bar{\varepsilon}_{19} \times \varepsilon_{20}$) from the track selection
365 conditions described in section 4.2 (Fig. 10). An example of the angular distribution of
366 the fill factor $\varepsilon_j(\theta_x, \theta_y)$ and muon detection efficiency $\epsilon(\theta_x, \theta_y)$ in an ECC is shown in
367 Fig. 11. The statistics of observed muons were limited in some angular bins by the
368 thick volcanic cone. However, the statistics were sufficient in the backward region (i.e.,
369 elevation angle < 0.0). We used the distribution of the negative elevation angular
370 region instead of the positive region, because it has enough statistics and the optics of
371 the HTS has an approximately two-fold rotational symmetry.

372



373

374



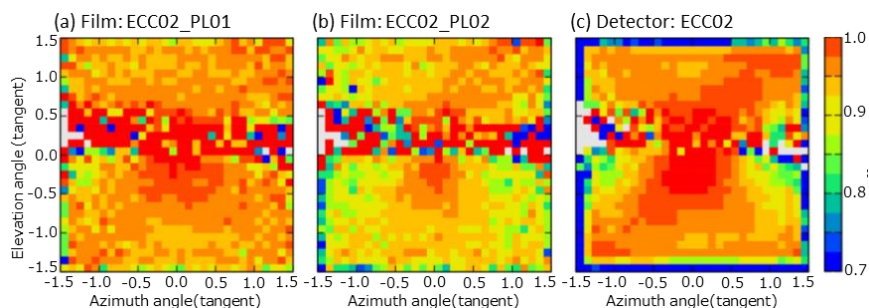
375

376 Figure 10. Example of all hit patterns and the products of fill factors in Eq. (4) when
 377 base tracks are found in film ID numbers 4 and 8. The red lines indicate the
 378 reconstructed tracks and the short black lines represent the base tracks found in the
 379 films.

380



381



382

383 Figure 11. Examples of the angular distribution of the fill factor in some films and the
384 efficiency of an ECC. (a) Fill factor for film ID = PL01 (most upstream film) and ECC
385 ID = 02 at site “N”. (b) Fill factor for film ID = PL02 and ECC ID = 02. (c) Muon
386 detection efficiency for ECC ID = 02 as evaluated by Eq. (4). The horizontal axis is the
387 tangent of azimuth angle; the vertical axis is the tangent of the elevation angle; the
388 colors represent the fill factor/efficiency values. A positive elevation angle means the
389 muon path is from the cone; a negative elevation angle means the muon path is from
390 the backward free sky. The gray color means there were no observed muons in the
391 angular bin due to the thick volcanic cone.

392



393 **5 Results**

394 The average density along muon path was determined for each observation site. We
395 used the muon flux model of Honda et al. (2004), energy loss model of Groom et al.
396 (2001), and topography around the Izu–Omuroyama scoria cone from the Geospatial
397 Information Authority of Japan (<https://maps.gsi.go.jp/>). The coordinates of the
398 observation site, direction, sensitive area, thickness of the ECC detectors, and
399 observation time were used to calculate the expected number of muons at each
400 observation site. The expected number of muons can be calculated as a function of the
401 average density ρ_k along the path:

$$402 \quad N_k^{simu}(\rho_k) = f_k(\rho_k, L_k) \times S_k \times \Omega_k \times T \times \epsilon_k \quad (5)$$

403 where k is the index of an angular bin, $f_k(\rho_k, L_k)$ is the penetrating muon flux
404 (calculated from the muon flux model, energy loss model, and path length L_k), S_k is the
405 sensitive area of the ECC, Ω_k is the solid angle, ϵ_k is the muon detection efficiency, and
406 T is the observation time.

407 The angular bin size used for calculating the expected value was $(0.01)^\circ$ in terms of
408 the tangent. The angular bins were then merged to improve the statistical accuracy of
409 the observed values. This merging procedure is useful in topology where a small
410 change in elevation angle can dramatically change the path length in the volcano. If k
411 is the index of the angular bins of $(0.01)^\circ$ and the bins belong to a larger angular bin i ,
412 then the following equation holds:

$$413 \quad N_i^{merged}(\rho_i) = \sum_k N_k^{simu}(\rho_i) \quad (6)$$

414 where ρ_i is the density of the merged angular bin i . If N_i^{obs} is the number of the
415 detected muons in the angular bin i , then we can uniquely determine the density value



416 ρ_i , such that $N_i^{merged}(\rho_i) = N_i^{obs}$. The lower limit ρ_i^{low} and upper limit ρ_i^{up} caused by the
417 statistical error on N_i^{obs} can also be estimated as follows:

$$418 \quad N_i^{merged}(\rho_i^{low}) = N_i^{obs} + \sqrt{N_i^{obs}} \quad (7)$$

$$419 \quad N_i^{merged}(\rho_i^{up}) = N_i^{obs} - \sqrt{N_i^{obs}} \quad (8)$$

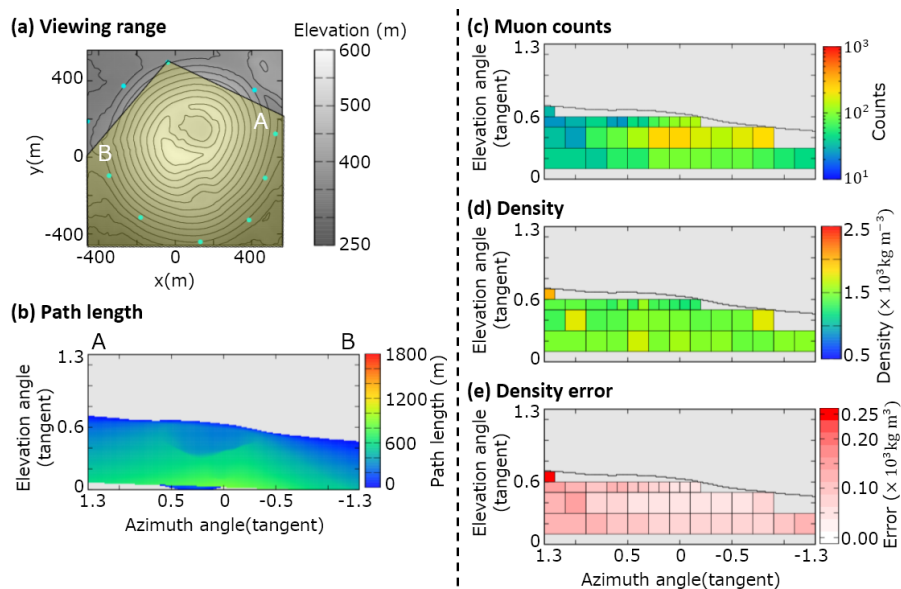
420 An example of the derived density map is shown in Fig. 12. All results are shown in
421 Figs 14–23 (Appendix A).

422 The definition of the angular bin areas was based on the following. The size of the
423 angular bins was $(0.2)^2$ when the elevation angle is 0.1 to 0.5 in tangent terms. When
424 the elevation angle is >0.5 , the angular bin size was $(0.1)^2$. If the observed muon count
425 in the bin was <25 , the angular bin was manually merged with adjacent bins to
426 improve the statistical error. The angular bin with a near-surface path (path length $<$
427 30 m) was excluded to avoid ambiguity between the actual topography and digital
428 elevation map. The attitude errors of each muon detector also contribute to the path
429 length ambiguity, especially near the surface of the cone.

430



431



432

433

434 Figure 12. Data for observation site N. (a) Map, topography, and viewing range; (b)
 435 path length of the volcanic cone; (c) muon counts N_i^{obs} ; (d) density ρ_i . The maximum
 436 value of the color bar indicates a density of $>2.5 \times 10^3 \text{ kg m}^{-3}$ and the minimum value
 437 is $<0.5 \times 10^3 \text{ kg m}^{-3}$. (e) Density error $\Delta\rho = (\rho_i^{up} - \rho_i^{low})/2$. The maximum value of the
 438 color bar indicates a density error of $>0.25 \times 10^3 \text{ kg m}^{-3}$.

439



440 **6 Validation**

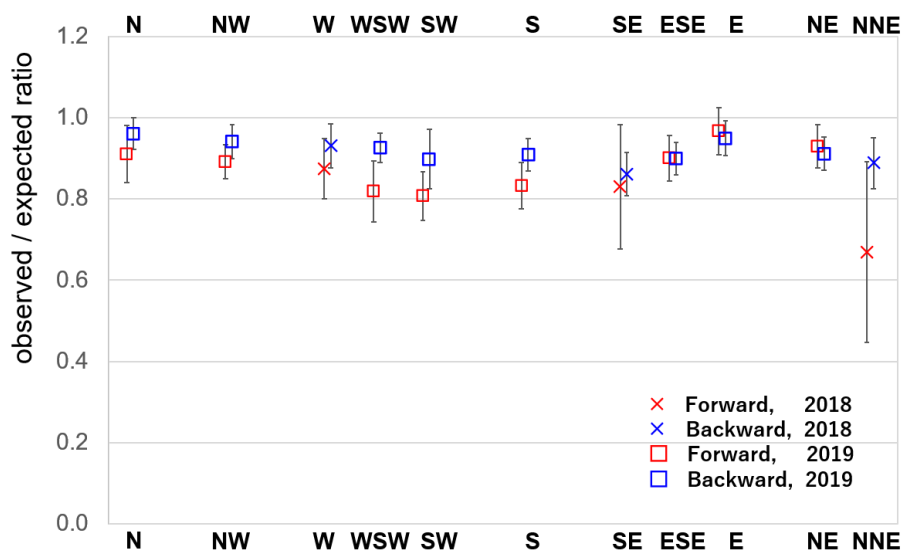
441 Firstly, we validated the observed muon flux by comparing it with the muon flux
442 model in the free sky region. The average and standard deviation of the ratio between
443 the sites were $88\% \pm 4\%$ in the forward direction and $92\% \pm 2\%$ in the backward
444 direction, except for the NNE site (Fig. 13). There were also 4%–7% in each detector
445 site except the forward directions at the SE and NNE site (Fig. 14). For reference, a
446 10% error on the flux corresponds to a 4% error on the density length at a $\tan(\text{elevation}$
447 $\text{angle}) = 0.2$ and density length = 1000 m (water equivalent). These deviations were
448 less than the errors caused by the muon statistics. The discrepancy for the NNE site is
449 discussed in the next section.

450 Secondly, we compared the density of the entire volcanic cone determined by gravity
451 data with that obtained by muography. Table 2 shows the density determined from
452 each observation site when the cone is considered to be uniform. The calculation of the
453 overall density $\bar{\rho}$ is as follows:

454
$$\bar{\rho} = \frac{\sum_i \rho_i V_i}{\sum_i V_i} \quad (9)$$

455 where i is the index of the angular bins and V_i is the volume of the volcanic cone cut off
456 by the angle bin i . Based on the gravity study of Nishiyama et al. (2021), the density of
457 the Izu–Omuroyama scoria cone is $1.39 \pm 0.07 \times 10^3 \text{ kg m}^{-3}$. The overall density
458 derived by muography at each observation site is $1.42\text{--}1.53 \times 10^3 \text{ kg m}^{-3}$, except for
459 one site. These values are broadly consistent with the density determined from gravity
460 data, except for the observation site W ($1.72 \times 10^3 \text{ kg m}^{-3}$).

461



462

463 Figure 13. The observed/expected muon flux ratio for each observation site in the

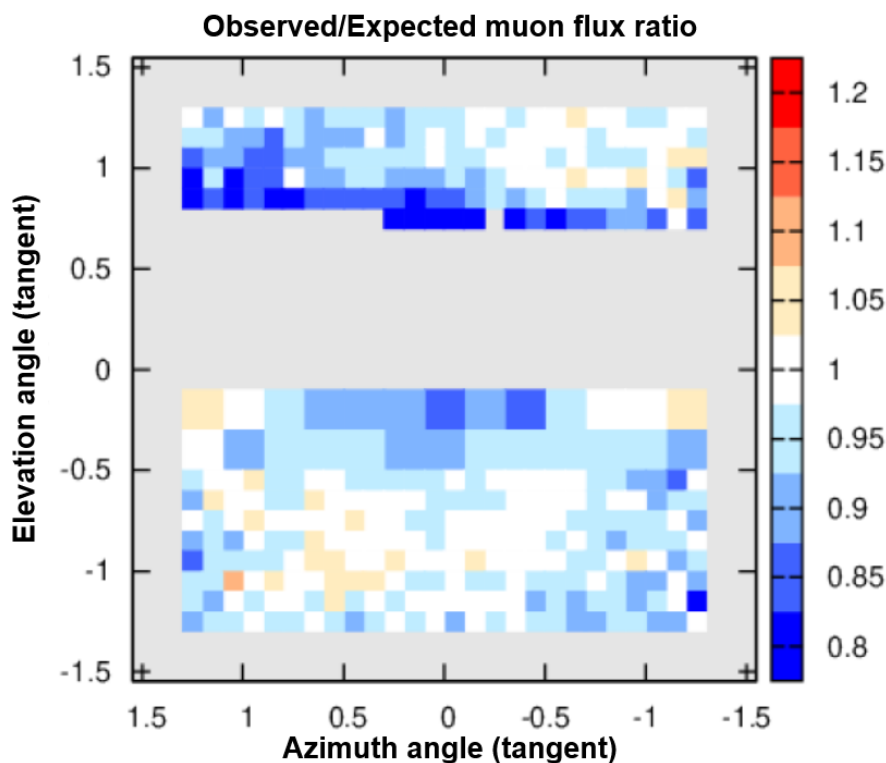
464 free sky region. The plot represents the average value of the ratio in tangential

465 angular space, and the error bars are the standard deviations at each site.

466



467



468

469

470 Figure 14. Example of the observed/expected muon flux ratio in the free sky region at
471 site N. The horizontal axis represents azimuth angle, and the vertical axis represents
472 the elevation angle. Positive elevation angle means the muons come from forward
473 directions (the volcanic cone). Negative elevation angle means the muons come from
474 backward free sky directions. Typical deviation of the ratio is 4%–7% in each site.

475

476



477

Observation site	Overall density $\bar{\rho}$ ($\times 10^3$ kg m $^{-3}$)	Observation site	Overall density $\bar{\rho}$ ($\times 10^3$ kg m $^{-3}$)
N	1.51	S	1.49
NW	1.45	ESE	1.45
W	1.72	E	1.42
WSW	1.50	NE	1.53
SE	1.46	NNE	1.50
SW	1.48		

478 Table 2. Overall bulk density obtained by muography, assuming that the density is

479 uniform in the volcanic cone.

480



481 **7 Discussion**

482 For the observed/expected muon flux ratio in the free sky region, the values in the
483 forward direction are less than in the backward direction at many observation sites.

484 This could be because the detectors were buried in holes on steep slopes ($\sim 30^\circ$), and our
485 analysis might not account for that effect. Due to the steep slope, muons arriving from
486 the forward direction need to penetrate some amount of soil, whereas muons from the
487 backward direction can enter the detector without being affected by the soil cover. In
488 addition, the resolution of the detector coordinates is ~ 3 m, which might also contribute
489 to the discrepancy.

490 Some density results from near the ground surface are complex. Some regions near the
491 path length of 30 m appear to have relatively higher or lower density than the other
492 data (e.g., Fig. A6, A9). One possible reason for this is the error on the detector
493 attitude. Near the surface of the volcanic cone, the difference between the calculated
494 and actual path lengths may become larger due to the error on the detector attitude.

495 The anomalous data for the NNE site also warrants further consideration. The reason
496 for this might be a difference between the digital elevation map and actual topography.
497 There is a stone wall in front of the buried detector at this site, which is about 1 m high
498 and located on the volcanic cone side. The grid size of the digital elevation map used in
499 this study is 1 m, and thus the map might not record this steep gradient.

500 In summary, errors in the position and attitude of the detectors, and the accuracy of
501 the DEM, might cause a misfit between the DEM and actual topography. These are the
502 main reasons for the discrepancy between the observed and expected muon flux.

503 The discrepancy between the observed and expected muon flux was $\pm 4\%$ in the
504 forward direction and $\pm 2\%$ in the backward direction between the detectors. In



505 addition, the typical deviation inside each site was 4%–7%. These values are smaller
506 than the statistical error of the observed muons used to determine the density of the
507 volcanic cone, and thus they were not significant for our observations. It is interesting
508 to consider if an improvement in the accuracy of the detector position and attitude, and
509 the DEM, would decrease this systematic error. For example, the $\pm 4\%$ deviation in the
510 forward direction would be expected to decrease to $\pm 2\%$, because the misfit effect is
511 less in the backward direction. Further improvements will require simulation of the
512 expected muon flux that take into account more processes and verification of the
513 systematic errors associated with the ECC detectors.

514 The obtained density values ($1.42\text{--}1.53 \times 10^3 \text{ kg m}^{-3}$; this study) and 1.39 ± 0.07
515 $\times 10^3 \text{ kg m}^{-3}$ (Nishiyama et al., 2021) for Izu–Omuroyama scoria cone are broadly
516 consistent (Table 2). In a previous study, Rosas-Carbajal et al. (2017) identified an
517 offset between the density obtained by muon and gravity data and the density obtained
518 from muon data was $0.5 \times 10^3 \text{ kg m}^{-3}$ less than that obtained from gravity data. In our
519 validation, this discrepancy does not exist. As Rosas-Carbajal et al (2017) suggested,
520 the discrepancy might be due to differences in the filtering performance for low-
521 momentum particles shown in Fig. 9.

522 The higher density obtained at site W cannot be explained by the systematic errors
523 described above. One possible reason for this is an actual high-density structure in
524 front of the site. This hypothesis is consistent with the fact that lava flowed out from
525 the crater lake to the west (Koyano et al., 1996).

526



527 **8 Conclusions**

528 A muographic study of the Izu–Omuroyama scoria cone was undertaken in 11
529 directions. The ECC detector design was optimized for quick installation in the field.
530 We mounted the 11 detectors beneath the ground, surrounding the volcanic cone. The
531 tracks of charged particles that passed through the ECCs were reconstructed using the
532 automated emulsion track readout system HTS and NETSCAN 2.0 software. After
533 track selection, including momentum filtering and efficiency estimation, the density
534 profiles in 2D angular space were derived for each observation site. The methods
535 described in this paper can be applied to the observation of other volcanoes and target
536 objects.

537 We compared the observed muon flux to the expected value from a muon flux model in
538 the free sky region. The muon flux difference between each detector was 4% in the
539 forward directions and 2% in the backward directions, and the typical deviations in
540 each site were about 4%–7%. The errors on the detector coordinates and attitude, and
541 DEM, are the main cause of the discrepancy between the observed and expected muon
542 flux.

543 In addition, we also compared our results with the overall volcanic cone density
544 estimated from gravity data, which are broadly consistent, apart from the W site. This
545 discrepancy for the W site can be explained by the systematic errors discussed in the
546 previous section and statistical error of the observed muons. It might also reflect a
547 high-density structure located in the western flank of the volcano. Further 3D density
548 reconstructions of the Izu–Omuroyama scoria cone are ongoing using the data set
549 described in this paper.

550



551 **Acknowledgements**

552 The authors thank Hideaki Aoki and his colleagues of Ike-kankou for collaborating on
553 our study. We also thank Masakazu Ichikawa of the Earthquake Research Institute,
554 the University of Tokyo, for support during the observation campaign. We are also
555 grateful for the technical support of the staff and students in F-lab, Nagoya University,
556 especially with the nuclear emulsion films. This research was supported by JSPS
557 KAKENHI Grant 19H01988, an Izu Peninsula Geopark Academic Research Grant
558 (2018), the Joint Research Program of the Institute of Materials and Systems for
559 Sustainability at Nagoya University (2017–2021), and a JSPS Fellowship (Nagahara;
560 Grant DC2, 19J13805).
561



562 **References**

- 563 Agafonova, N., Aleksandrov, A., Altinok, O., Anokhina, A., Aoki, S., Ariga, A., Ariga, T.,
564 Autiero, D., Badertscher, A., Bagulya, A., Ben Dhahbi, A., Bertolin, A., Besnier, M.,
565 Bozza, C., Brugière, T., Brugnera, R., Brunet, F., Brunetti, G., Buontempo, S., Cazes,
566 A., Chaussard, L., Chernyavskiy, M., Chiarella, V., Chukanov, A., D'Ambrosio, N., Dal
567 Corso, F., De Lellis, G., del Amo Sanchez, P., Déclais, Y., De Serio, M., Di Capua, F., Di
568 Crescenzo, A., Di Ferdinando, D., Di Marco, N., Dmitrievski, S., Dracos, M.,
569 Duchesneau, D., Dusini, S., Dzhatdoev, T., Ebert, J., Egorov, O., Enikeev, R., Ereditato,
570 A., Esposito, L. S., Favier, J., Ferber, T., Fini, R. A., Frekers, D., Fukuda, T.,
571 Garfagnini, A., Giacomelli, G., Giorgini, M., Göllnitz, C., Goldberg, J., Golubkov, D.,
572 Goncharova, L., Gornushkin, Y., Grella, G., Grianti, F., Guler, A. M., Gustavino, C.,
573 Hagner, C., Hamada, K., Hara, T., Hierholzer, M., Hollnagel, A., Hoshino, K., Ieva, M.,
574 Ishida, H., Jakovcic, K., Jollet, C., Juget, F., Kamiscioglu, M., Kazuyama, K., Kim, S.
575 H., Kimura, M., Kitagawa, N., Klicek, B., Knuesel, J., Kodama, K., Komatsu, M., Kose,
576 U., Kreslo, I., Kubota, H., Lazzaro, C., Lenkeit, J., Lippi, I., Ljubcic, A., Longhin, A.,
577 Loverre, P., Lutter, G., Malgin, A., Mandrioli, G., Manai, K., Marteau, J., Matsuo, T.,
578 Matveev, V., Mauri, N., Medinaceli, E., Meisel, F., Meregaglia, A., Migliozi, P.,
579 Mikado, S., Miyamoto, S., Monacelli, P., Morishima, K., Moser, U., Muciaccia, M. T.,
580 Naganawa, N., Naka, T., Nakamura, M., Nakano, T., Naumov, D., Nikitina, V., Niwa,
581 K., Nonoyama, Y., Ogawa, S., Okateva, N., Olshevskiy, A., Paniccia, M., Paoloni, A.,
582 Park, B. D., Park, I. G., Pastore, A., Patrizii, L., Pennacchio, E., Pessard, H., Pretzl, K.,
583 Pilipenko, V., Pistillo, C., Polukhina, N., Pozzato, M., Pupilli, F., Rescigno, R.,
584 Roganova, T., Rokujo, H., Romano, G., Rosa, G., Rostovtseva, I., Rubbia, A., Russo, A.,
585 Ryasny, V., Ryazhskaya, O., Sato, O., Sato, Y., Schembri, A., Schmidt-Parzefall, W.,



586 Schroeder, H., Scotto Lavina, L., Sheshukov, A., Shibuya, H., Shoziyoev, G., Simone, S.,
587 Sioli, M., Sirignano, C., Sirri, G., Song, J. S., Spinetti, M., Stanco, L., Starkov, N.,
588 Stipcevic, M., Strauss, T., Strolin, P., Takahashi, S., Tenti, M., Terranova, F., Tezuka,
589 I., Tioukov, V., Tolun, P., Trabelsi, A., Tran, T., Tufanli, S., Vilain, P., Vladimirov, M.,
590 Votano, L., Vuilleumier, J. L., Wilquet, G., Wonsak, B., Yakushev, V., Yoon, C. S.,
591 Yoshioka, T., Yoshida, J., Zaitsev, Y., Zemsikova, S., Zghiche, A., and Zimmermann, R.:
592 Momentum measurement by the multiple Coulomb scattering method in the OPERA
593 lead-emulsion target, *New J. Phys.*, 14, 013026, [https://doi.org/10.1088/1367-](https://doi.org/10.1088/1367-2630/14/1/013026)
594 [2630/14/1/013026](https://doi.org/10.1088/1367-2630/14/1/013026), 2012.
595
596 Aramaki, S., and Hamuro, K.: Geology of the Higasi-Izu monogenetic volcano group,
597 *Bull. Earthq. Res. Inst. Univ. Tokyo*, 52, 235–278, [https://repository.dl.itc.u-](https://repository.dl.itc.u-tokyo.ac.jp/record/33207/files/ji0522010.pdf)
598 [tokyo.ac.jp/record/33207/files/ji0522010.pdf](https://repository.dl.itc.u-tokyo.ac.jp/record/33207/files/ji0522010.pdf), 1977. (in Japanese)
599
600 Bozza, C., D'Ambrosio, N., De Lellis, G., De Serio, M., Di Capua, F., Di Crescenzo, A.,
601 Di Ferdinando, D., Di Marco, N., Esposito, L. S., Rosa Anna Fini, R. A., Giacomelli, G.,
602 Grella, G., Ieva, M., Kose, U., Longhin, A., Mauri, N., Medinaceli, E., Monacelli, P.,
603 Muciaccia, M. T., Pastore, A., Patrizii, L., Pozzato, M., Pupilli, F., Rescigno, R.,
604 Romano, G., Rosa, G., Ruggieri, A., Russo, A., Simone, S., Sirignano, C., Sirri, G.,
605 Stellacci, S. M., Tenti, M., Tioukov, V., Togo, V., and Valieri, C.: An integrated system
606 for large scale scanning of nuclear emulsions, *Nucl. Instrum. Methods Phys. Res. A*,
607 703, 1, 204–212, <https://doi.org/10.1016/j.nima.2012.11.099>, 2012.
608
609 Bush, A. L.: Construction Materials: Lightweight Aggregates, in “Encyclopedia of



- 610 Materials: Science and Technology”, Elsevier, pp 1550–1558, <https://doi.org/10.1016/B0->
611 [08-043152-6/00277-1](https://doi.org/10.1016/B0-08-043152-6/00277-1), 2001.
- 612
- 613 Geshi, N., and Neri, M.: Dynamic feeder dyke systems in basaltic volcanoes: the
614 exceptional example of the 1809 Etna eruption (Italy), *Front. Earth Sci.*, 2, 13,
615 <https://doi.org/10.3389/feart.2014.00013>, 2014.
- 616
- 617 Groom, D. E., Mokhov, N. V., and Striganov, S. I.: Muon stopping power and range
618 tables 10 MeV–100 TeV, *At. Data Nucl. Data Tables*, 78, 183–356,
619 <https://doi.org/10.1006/adnd.2001.0861>, 2001.
- 620
- 621 Hamada, K., Fukuda, T., Ishiguro, K., Kitagawa, N., Kodama, K., Komatsu, M.,
622 Morishima, K., Nakano, T., Nakatsuka, Y., Nonoyama, Y., Sato, O., and Yoshida, J.:
623 Comprehensive track reconstruction tool “NETSCAN 2.0” for the analysis of the
624 OPERA Emulsion Cloud Chamber, *J. Instrum.*, 7, P07001, <https://doi.org/10.1088/1748->
625 [0221/7/07/P07001](https://doi.org/10.1088/1748-0221/7/07/P07001), 2012.
- 626
- 627 Hamuro, K.: Petrology of the Higashi–Izu monogenetic volcano group, *Bull. Earthq.*
628 *Res. Inst. Univ. Tokyo*, 60, 335–400, [https://repository.dl.itc.u-](https://repository.dl.itc.u-tokyo.ac.jp/record/32886/files/ji0603001.pdf)
629 [tokyo.ac.jp/record/32886/files/ji0603001.pdf](https://repository.dl.itc.u-tokyo.ac.jp/record/32886/files/ji0603001.pdf), 1985.
- 630
- 631 Hiramoto, A., Suzuki, Y., Ali, A., Aoki, S., Berns, L., Fukuda, T., Hanaoka, Y., Hayato,
632 Y., Ichikawa, A. K., Kawahara, H., Kikawa, T., Koga, T., Komatani, R., Komatsu, M.,
633 Kosakai, Y., Matsuo, T., Mikado, S., Minamino, A., Mizuno, K., Morimoto, Y.,



- 634 Morishima, K., Naganawa, N., Naiki, M., Nakamura, M., Nakamura, Y., Nakano, N.,
635 Nakano, T., Nakaya, T., Nishio, A., Odagawa, T., Ogawa, S., Oshima, H., Rokujo, H.,
636 Sanjana, I., Sato, O., Shibuya, H., Sugimura, K., Suzui, L., Takagi, H., Takao, T.,
637 Tanihara, Y., Yasutome, K., and Yokoyama, M. (NINJA Collaboration): First
638 measurement of ν_{μ} and $\bar{\nu}_{\mu}$ charged-current inclusive interactions on water using a
639 nuclear emulsion detector, Phys. Rev. D, 102, 072006,
640 <https://doi.org/10.1103/PhysRevD.102.072006>, 2020.
641
642 Honda, M., Kajita, T., Kasahara, K., and Midorikawa, S.: New calculation of the
643 atmospheric neutrino flux in a three-dimensional scheme, Phys. Rev. D, 70, 043008,
644 <https://doi.org/10.1103/PhysRevD.70.043008>, 2004.
645
646 Jourde, K., Gibert, D., and Marteau, J.: Improvement of density models of geological
647 structures by fusion of gravity data and cosmic muon radiographies, Geosci. Instrum.
648 Methods Data Syst., 4, 177–188, <https://doi.org/10.5194/gi-4-177-2015>, 2015.
649
650 Jourde, K., Gibert, D., Marteau, J., d'Ars, J.B., and Komorowski, J.C.: Muon dynamic
651 radiography of density changes induced by hydrothermal activity at the La Soufrière of
652 Guadeloupe volcano, Sci. Rep., 6, 33406, <https://doi.org/10.1038/srep33406>, 2016.
653
654 Kereszturi, G., and Németh, K.: Monogenetic Basaltic Volcanoes: Genetic
655 Classification, Growth, Geomorphology and Degradation, Updates in Volcanology—
656 New Advances in Understanding Volcanic Systems, Karoly Nemeth, IntechOpen., DOI:
657 10.5772/51387, 2012.



658

659 Kodama, K., Hoshino, K., Komatsu, M., Miyanishi, M., Nakamura, M., Nakamura, T.,
660 Nakano, T., Narita, K., Niwa, K., Nonaka, N., Sato, O., Toshito, T., and Uetake, T.:
661 Study of electron identification in a few GeV region by an emulsion cloud chamber,
662 Rev. Sci. Instrum., 74, 53, <https://doi.org/10.1063/1.1529300>, 2003.

663

664 Koyama, M.: Photographs of the Izu-peninsula by UAV, Iwanami Science Library 268,
665 Iwanami Shoten, Publishers, Tokyo, 159 pp, ISBN 9784000296687, 2017. (in Japanese)

666

667 Koyano, Y., Hayakawa, Y., and Machida, H.: The eruption of Omuroyama in the
668 Higashi Izu monogenetic volcano field, J Geog. (Chigaku Zasshi), 105, 4, 475–484,
669 <https://doi.org/10.5026/jgeography.105.4.475>, 1996. (in Japanese)

670

671 Kreslo, I., Cozzi, M., Ereditato, A., Hess, M., Knuesel, J., Laktineh, I., Messina, M.,
672 Moser, U., Pistillo, C., and Pretzl, K.: High-speed analysis of nuclear emulsion films
673 with the use of dry objective lenses, J. Instrum., 3, P04006,
674 <https://dx.doi.org/10.1088/1748-0221/3/04/P04006>, 2008.

675

676 Morishima, K., and Nakano, T.: Development of a new automatic nuclear emulsion
677 scanning system, S-UTS, with continuous 3D tomographic image read-out, J. Instrum.,
678 5, P04011, <http://dx.doi.org/10.1088/1748-0221/5/04/P04011>, 2010.

679

680 Morishima, K., Kuno, M., Nishio, A., Kitagawa, N., Manabe, Y., Moto, M., Takasaki, F.,
681 Fujii, H., Satoh, K., Kodama, H., Hayashi, K., Odaka, S., Procureur, S., Attie, D.,



682 Bouteille, S., Calvet, D., Filosa, C., Magnier, P., Mandjavidze, I., Riallot, M., Marini, B.,
683 Gable, P., Date, Y., Sugiura, M., Elshayeb, Y., Elnady, T., Ezzy, M., Guerriero, E.,
684 Steiger, V., Serikoff, N., Mouret, J., Charles, B., Helal, H., and Tayoubi, M.: Discovery
685 of a big void in Khufu's Pyramid by observation of cosmic-ray muons, *Nature*, 552, 387,
686 <https://doi.org/10.1038/nature24647>, 2017.
687
688 Nagahara, S., and Miyamoto, S.: Feasibility of three-dimensional density tomography
689 using dozens of muon radiographies and filtered back projection for volcanoes, *Geosci.*
690 *Instrum. Methods Data Syst.*, 7, 307–316, <https://doi.org/10.5194/gi-7-307-2018>, 2018.
691
692 Nakamura, T., Ariga, A., Ban, T., Fukuda, T., Fukuda, T., Fujioka, T., Furukawa, T.,
693 Hamada, K., Hayashi, H., Hiramatsu, S., Hoshino, K., Kawada, J., Koike, N., Komatsu,
694 M., Matsuoka, H., Miyamoto, S., Miyanishi, K., Miyanishi, M., Morishima, K., Nada,
695 H., Naganawa, N., Nakano, T., Narita, K., Natsume, M., Niwa, K., Nonaka, N., Park,
696 B. D., Sato, O., Takahashi, S., Toshito, T., Uetake, T., Nakamura, M., Kuwabara, K.,
697 Nishiyama, S., Nonoyama, Y., and Kodama, K.: The OPERA film: New nuclear
698 emulsion for large-scale, high-precision experiments, *Nucl. Instrum. Methods Phys.*
699 *Res. A*, 556, 1, 80–86, <https://doi.org/10.1016/j.nima.2005.08.109>, 2005.
700
701 Nishio, A., Morishima, K., Kuwabara, K., Yoshida, T., Funakubo, T., Kitagawa, N.,
702 Kuno, M., Manabe, Y., and Nakamura, M.: Nuclear emulsion with excellent long-term
703 stability developed for cosmic-ray imaging, *Nuclear Instruments and Methods in*
704 *Physics Research A*, 966, 163850, <https://doi.org/10.1016/j.nima.2020.163850>, 2020.
705



- 706 Nishiyama, R., Miyamoto, S., and Naganawa, N.: Experimental study of source of
707 background noise in muon radiography using emulsion film detectors, *Geosci. Instrum.*
708 *Methods Data Syst.*, 3, 29–39, <https://doi.org/10.5194/gi-3-29-2014>, 2014.
- 709
- 710 Nishiyama, R., Miyamoto, S., Okubo, S., Oshima, H., and Maekawa, T.: 3D density
711 modeling with gravity and muon-radiographic observations in Showa–Shinzan lava
712 dome, Usu, Japan, *Pure Appl. Geophys.*, 174, 1061–1070,
713 <https://doi.org/10.1007/s00024-016-1430-9>, 2017.
- 714
- 715 Nishiyama, R., Miyamoto, S., and Nagahara, S.: Estimation of the bulk density of the
716 Omuro scoria cone (eastern Izu, Japan) from gravity survey, *Bull. Earthq. Res. Inst.*
717 *Univ. Tokyo*, 95, 1–7, [https://repository.dl.itc.u-](https://repository.dl.itc.u-tokyo.ac.jp/record/2000093/files/IHO951401.pdf)
718 [tokyo.ac.jp/record/2000093/files/IHO951401.pdf](https://repository.dl.itc.u-tokyo.ac.jp/record/2000093/files/IHO951401.pdf), 2020.
- 719
- 720 Oláh, L., Tanaka, H. K. M., Ohminato, T., and Varga, D.: High-definition and low-noise
721 muography of the Sakurajima volcano with gaseous tracking detectors, *Sci. Rep.*, 8,
722 3207, <https://doi.org/10.1038/s41598-018-21423-9>, 2018.
- 723
- 724 Rosas-Carbajal, M., Jourde, K., Marteau, J., Deroussi, S., Komorowski, J.-C., and
725 Gibert, D.: Three-dimensional density structure of La Soufrière de Guadeloupe lava
726 dome from simultaneous muon radiographies and gravity data, *Geophys. Res. Lett.*, 44,
727 6743–6751, <https://doi.org/10.1002/2017GL074285>, 2017.
- 728
- 729 Saito, T., Takahashi, S., and Wada, H.: ^{14}C ages of Omuroyama Volcano, Izu Peninsula,



- 730 Bull. Volcanol. Soc. Jpn. , 48, 215–219, https://doi.org/10.18940/kazan.48.2_215, 2003.
- 731 (in Japanese)
- 732
- 733 Saracino, G., Amato, L., Ambrosino, F., Antonucci, G., Bonechi, L., Cimmino, L.,
734 Consiglio, L., D'Alessandro, R., De Luzio, E., Minin, G., Noli, P., Scognamiglio, L.,
735 Strolin, P., and Varriale, A.: Imaging of underground cavities with cosmic-ray muons
736 from observations at Mt. Echia (Naples), Sci. Rep., 7, 1181,
737 <https://doi.org/10.1038/s41598-017-01277-3>, 2017.
- 738
- 739 Taha, A. A., and Mohamed, A. A.: Chemical, physical and geotechnical properties
740 comparison between scoria and pumice deposits in Dhamar–Rada Volcanic Field, SW
741 Yemen, Aust. J. Basic & Appl. Sci., 7, 11, 116–124,
742 <http://www.ajbasweb.com/old/ajbas/2013/September/116-124.pdf>, 2013.
- 743
- 744 Takahashi, S., Aoki, S., Kamada, K., Mizutani, S., Nakagawa, R., Ozaki, K., and
745 Rokujo, H.: GRAINE project: The first balloon-borne, emulsion gamma-ray telescope
746 experiment, Prog. Theor. Exp. Phys., 4, <https://doi.org/10.1093/ptep/ptv046>, 2015.
- 747
- 748 Tanaka, H. K. M., Nakano, T., Takahashi, S., Yoshida, J., Takeo, M., Oikawa, J.,
749 Ohminato, T., Aoki, Y., Koyama, E., Tsuji, H., and Niwa, K.: High resolution imaging
750 in the inhomogeneous crust with cosmic-ray muon radiography: The density structure
751 below the volcanic crater floor of Mt. Asama, Japan, Earth Planet. Sci. Lett., 263, 1–2,
752 104–113, <https://doi.org/10.1016/j.epsl.2007.09.001>, 2007.
- 753



- 754 Tanaka, H. K. M., Uchida, T., Tanaka, M., Shinohara, H., and Hideaki, T.: Cosmic-ray
755 muon imaging of magma in a conduit: Degassing process of Satsuma–Iwojima Volcano,
756 Japan, *Geophys. Res. Lett.*, 36, L01304, <https://doi.org/10.1029/2008GL036451>, 2009.
757
- 758 Tanaka, H. K. M., Taira, H., Uchida, T., Tanaka, M., Takeo, M., Ohiminato, T., and
759 Tsuji, H.: Three-dimensional computational axial tomography scan of a volcano with
760 cosmic ray muon radiography, *J. Geophys. Res. Solid Earth*, 115, B12332,
761 <https://doi.org/10.1029/2010JB007677>, 2010.
762
- 763 Tanaka, H. K. M., Kusagaya, T., and Shinohara, H.: Radiographic visualization of
764 magma dynamics in an erupting volcano, *Nat. Commun.*, 5, 3381,
765 <https://doi.org/10.1038/ncomms4381>, 2014.
766
- 767 Tioukov, V., Alexandrov, A., Bozza, C., Consiglio, L., D’Ambrosio, N., De Lellis, G., De
768 Sio, C., Giudicepietro, F., Macedonio, G., Miyamoto, S., Nishiyama, R., Orazi, M.,
769 Peluso, R., Sheshukov, A., Sirignano, C., Stellacci, S. M., Strolin, P., and Tanaka, H. K.
770 M.: First muography of Stromboli volcano, *Sci. Rep.*, 9, 6695,
771 <https://doi.org/10.1038/s41598-019-43131-8>, 2019.
772
- 773 Watanabe, A., Takenaka, H., Fujii, Y., and Fujiwara, H.: Seismometer azimuth
774 measurement at K-NET station (2): Oita Prefecture, *Zisin*, 53, 185–192,
775 https://doi.org/10.4294/zisin1948.53.2_185, 2000. (in Japanese)
776
- 777 Yamamoto, H.: The mode of lava outflow from cinder cones in the Ojika–Jima



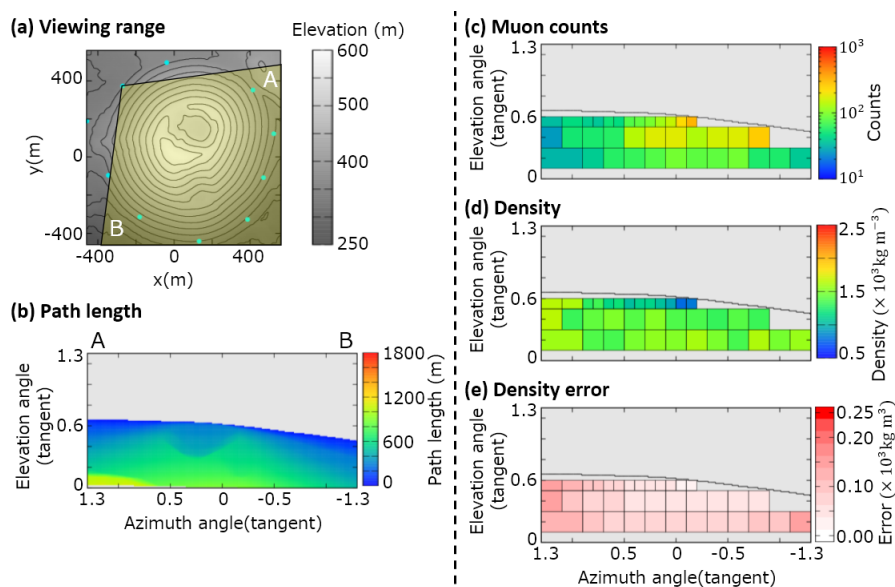
778 monogenetic volcano group, Bull. Volcanol. Soc. Jpn., 48, 1,
779 https://doi.org/10.18940/kazan.48.1_11, 2003. (in Japanese)
780
781 Yoshimoto, M., Nakano, T., Komatani, R., and Kawahara, H.: Hyper-track selector
782 nuclear emulsion readout system aimed at scanning an area of one thousand square
783 meters, Prog. Theor. Exp. Phys., 2017, 10, <https://doi.org/10.1093/ptep/ptx131>, 2017.
784



785 **Appendix A**

786 The density results for each observation site are shown in Figs 15–24.

787



788

789

790 Figure A1. Observation site NW. (a) Map, topography, and viewing range; (b) path

791 length of the volcanic cone; (c) muon counts N_i^{obs} ; (d) density ρ_i . The maximum value of

792 the color bar indicates a density of $>2.5 \times 10^3 \text{ kg m}^{-3}$ and the minimum value is <0.5

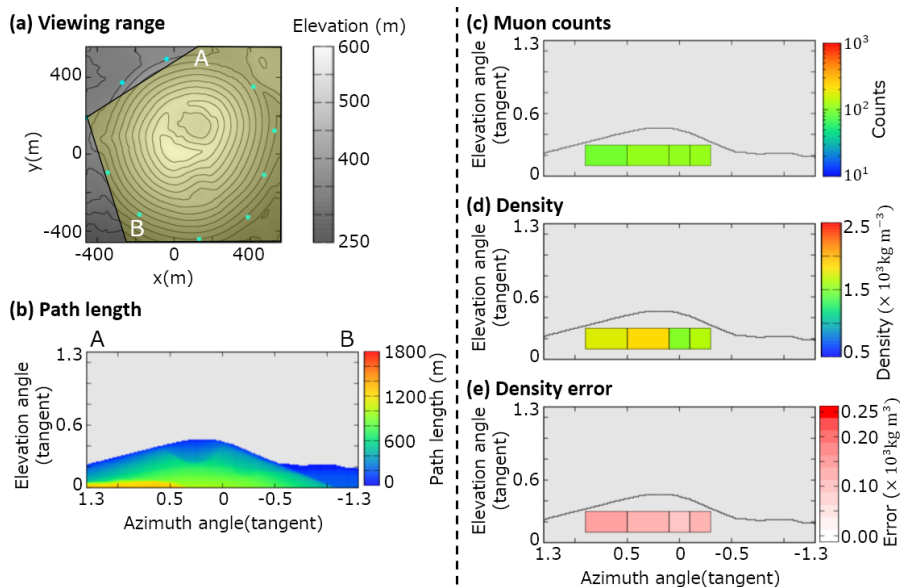
793 $\times 10^3 \text{ kg m}^{-3}$. (e) Density error $\Delta\rho = (\rho_i^{up} - \rho_i^{low})/2$. The maximum value of the color

794 bar indicates a density error of $>0.25 \times 10^3 \text{ kg m}^{-3}$.

795



796



797

798

799 Figure A2. Observation site W. (a) Map, topography, and viewing range; (b) path length

800 of the volcanic cone; (c) muon counts N_i^{obs} ; (d) density ρ_i . The maximum value of the

801 color bar indicates a density of $>2.5 \times 10^3 \text{ kg m}^{-3}$ and the minimum value is $<0.5 \times 10^3$

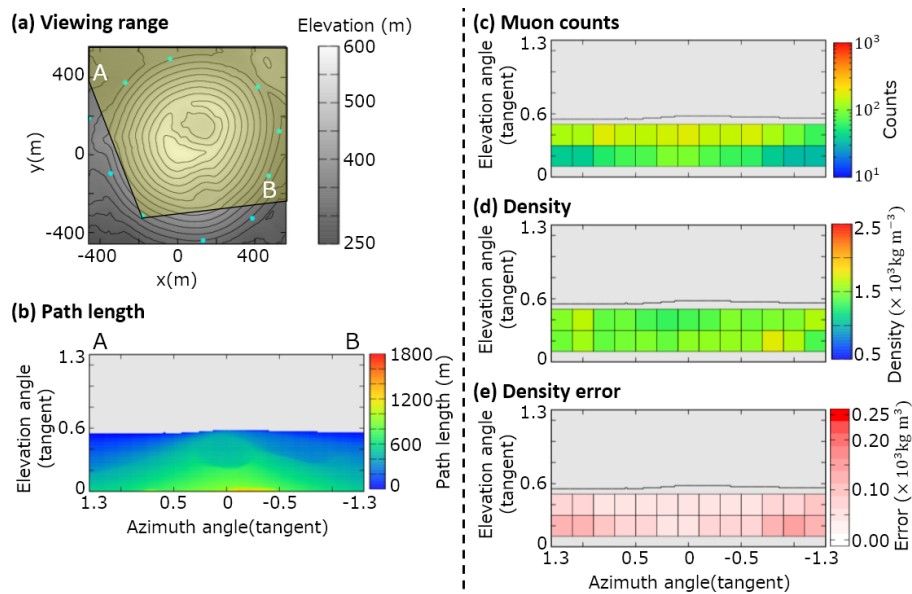
802 kg m^{-3} . (e) Density error $\Delta\rho = (\rho_i^{up} - \rho_i^{low})/2$. The maximum value of the color bar

803 indicates a density error of $>0.25 \times 10^3 \text{ kg m}^{-3}$.

804



805



806

807

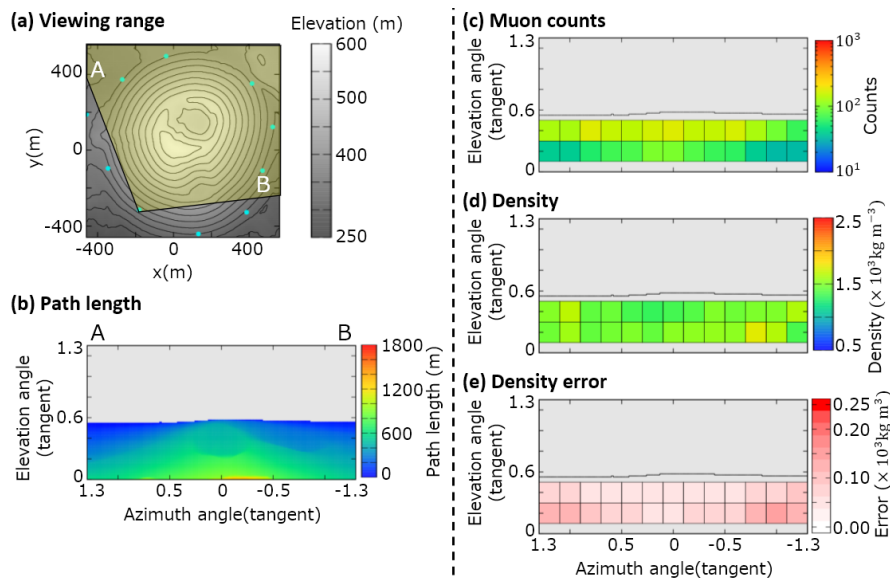
808 Figure A3. Observation site WSW. (a) Map, topography, and viewing range; (b) path
 809 length of the volcanic cone; (c) muon counts N_i^{obs} ; (d) density ρ_i . The maximum value of
 810 the color bar indicates a density of $>2.5 \times 10^3 \text{ kg m}^{-3}$ and the minimum value is <0.5
 811 $\times 10^3 \text{ kg m}^{-3}$. (e) Density error $\Delta\rho = (\rho_i^{up} - \rho_i^{low})/2$. The maximum value of the color
 812 bar indicates a density error of $>0.25 \times 10^3 \text{ kg m}^{-3}$.

813

814



815



816

817

818 Figure A4. Observation site SW. (a) Map, topography, and viewing range; (b) path
819 length of the volcanic cone; (c) muon counts N_i^{obs} ; (d) density ρ_i . The maximum value of of
820 the color bar indicates a density of $>2.5 \times 10^3 \text{ kg m}^{-3}$ and the minimum value is <0.5
821 $\times 10^3 \text{ kg m}^{-3}$. (e) Density error $\Delta\rho = (\rho_i^{up} - \rho_i^{low})/2$. The maximum value of the color
822 bar indicates a density error of $>0.25 \times 10^3 \text{ kg m}^{-3}$.

823

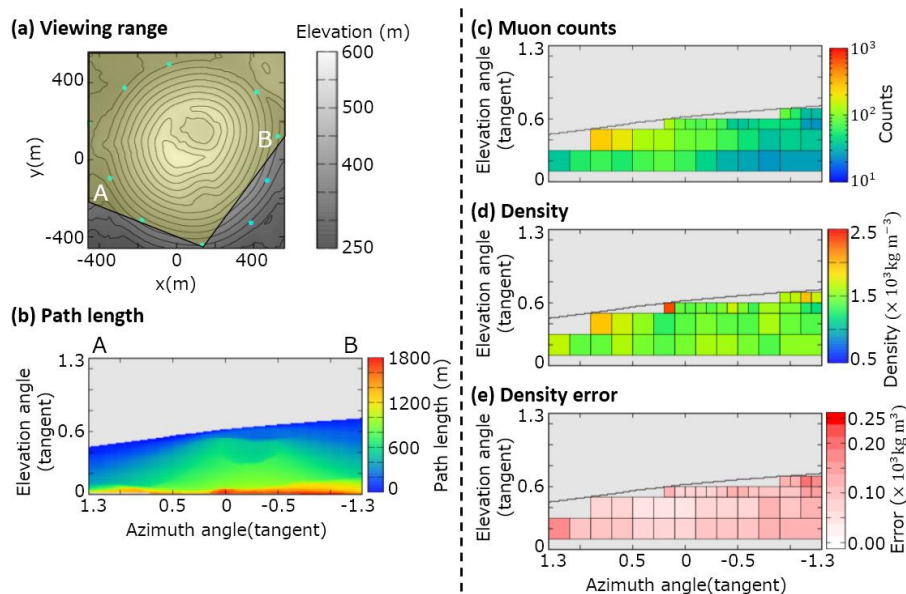
824

825

826



827



828

829

830 Figure A5. Observation site S. (a) Map, topography, and viewing range; (b) path length

831 of the volcanic cone; (c) muon counts N_i^{obs} ; (d) density ρ_i . The maximum value of the

832 color bar indicates a density of $>2.5 \times 10^3 \text{ kg m}^{-3}$ and the minimum value is $<0.5 \times 10^3$

833 kg m^{-3} . (e) Density error $\Delta\rho = (\rho_i^{up} - \rho_i^{low})/2$. The maximum value of the color bar

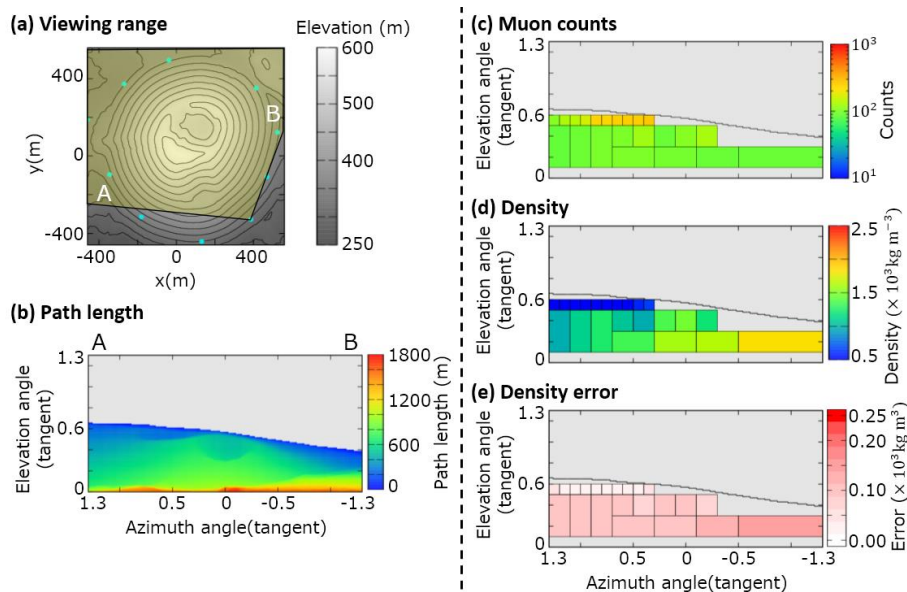
834 indicates a density error of $>0.25 \times 10^3 \text{ kg m}^{-3}$.

835

836



837



838

839

840 Figure A6. Observation site SE. (a) Map, topography, and viewing range; (b) path
 841 length of the volcanic cone; (c) muon counts N_i^{obs} ; (d) density ρ_i . The maximum value of
 842 the color bar indicates a density of $>2.5 \times 10^3 \text{ kg m}^{-3}$ and the minimum value is <0.5
 843 $\times 10^3 \text{ kg m}^{-3}$. (e) Density error $\Delta\rho = (\rho_i^{up} - \rho_i^{low})/2$. The maximum value of the color
 844 bar indicates a density error of $>0.25 \times 10^3 \text{ kg m}^{-3}$.

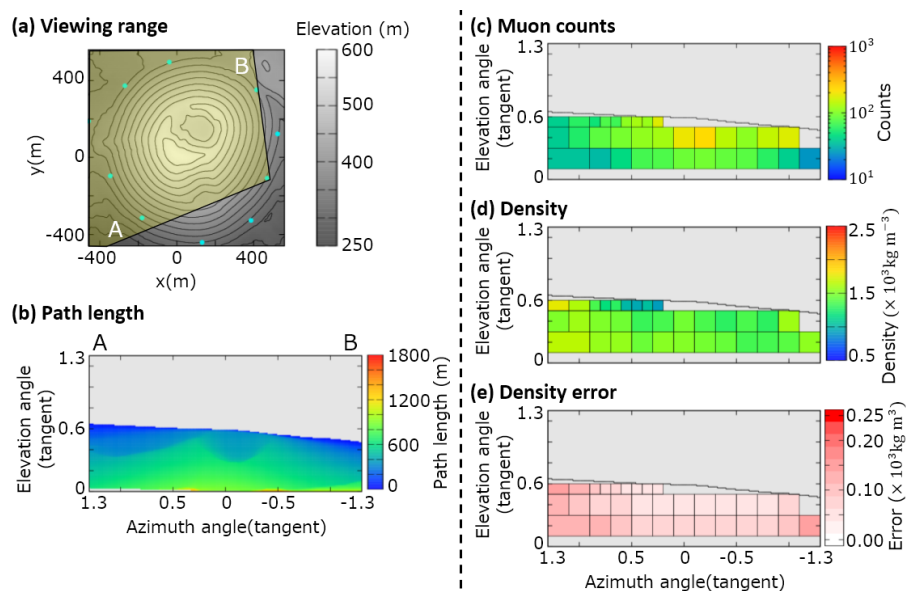
845

846

847



848



849

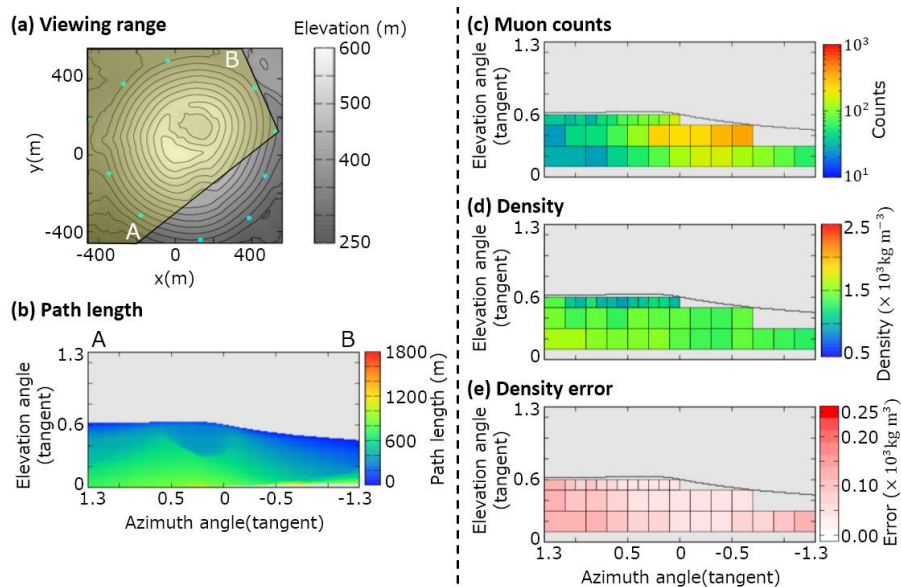
850

851 Figure A7. Observation site ESE. (a) Map, topography, and viewing range; (b) path
 852 length of the volcanic cone; (c) muon counts N_i^{obs} ; (d) density ρ_i . The maximum value of
 853 the color bar indicates a density of $>2.5 \times 10^3 \text{ kg m}^{-3}$ and the minimum value is <0.5
 854 $\times 10^3 \text{ kg m}^{-3}$. (e) Density error $\Delta\rho = (\rho_i^{up} - \rho_i^{low})/2$. The maximum value of the color
 855 bar indicates a density error of $>0.25 \times 10^3 \text{ kg m}^{-3}$.

856



857



858

859

860 Figure A8. Observation site E. (a) Map, topography, and viewing range; (b) path length

861 of the volcanic cone; (c) muon counts N_i^{obs} ; (d) density ρ_i . The maximum value of the

862 color bar indicates a density of $>2.5 \times 10^3 \text{ kg m}^{-3}$ and the minimum value is $<0.5 \times 10^3$

863 kg m^{-3} . (e) Density error $\Delta\rho = (\rho_i^{up} - \rho_i^{low})/2$. The maximum value of the color bar

864 indicates a density error of $>0.25 \times 10^3 \text{ kg m}^{-3}$.

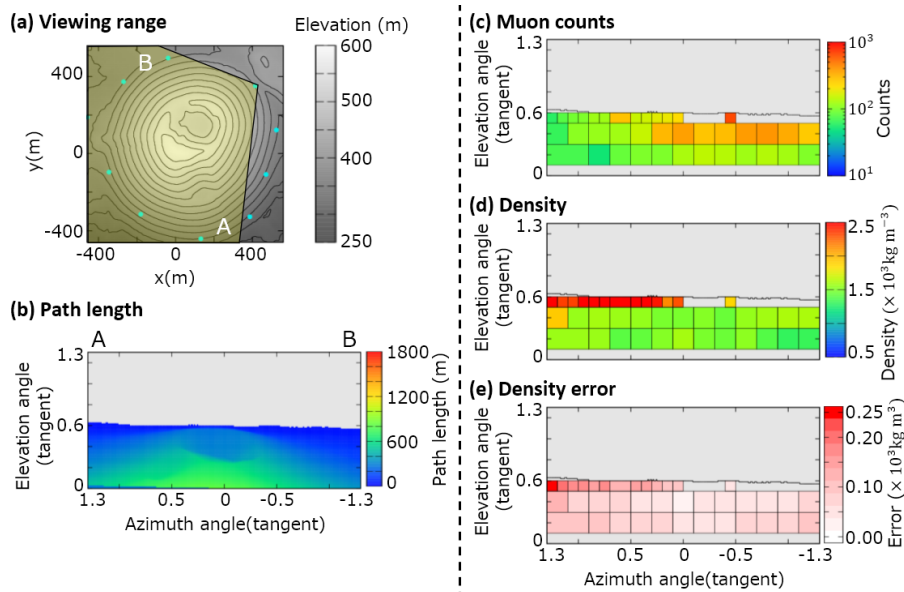
865

866

867



868



869

870

871 Figure A9. Observation site NE. (a) Map, topography, and viewing range; (b) path
 872 length of the volcanic cone; (c) muon counts N_i^{obs} ; (d) density ρ_i . The maximum value of
 873 the color bar indicates a density of $>2.5 \times 10^3 \text{ kg m}^{-3}$ and the minimum value is <0.5
 874 $\times 10^3 \text{ kg m}^{-3}$. (e) Density error $\Delta\rho = (\rho_i^{up} - \rho_i^{low})/2$. The maximum value of the color
 875 bar indicates a density error of $>0.25 \times 10^3 \text{ kg m}^{-3}$.

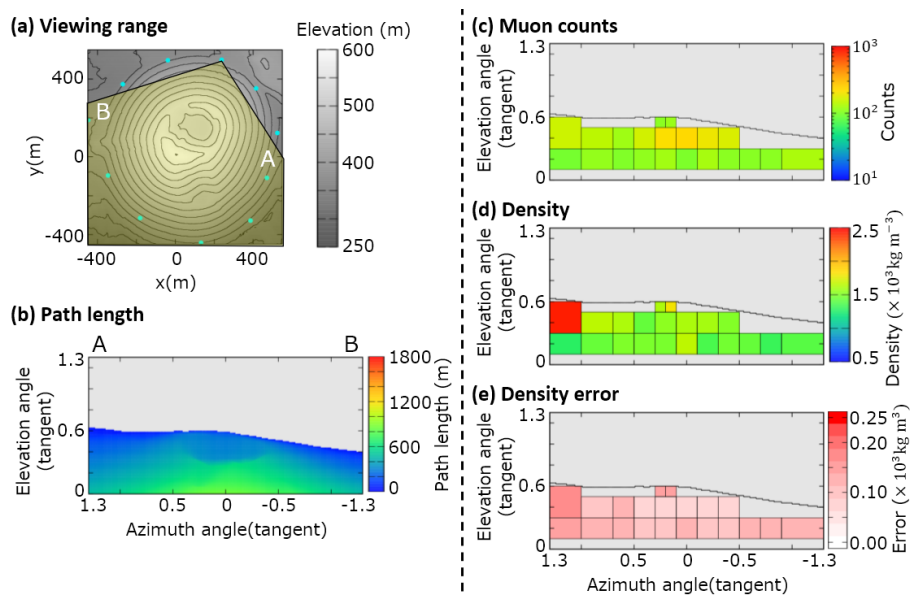
876

877

878



879



880

881

882 Figure A10. Observation site NNE. (a) Map, topography, and viewing range; (b) path
 883 length of the volcanic cone; (c) muon counts N_i^{obs} ; (d) density ρ_i . The maximum value of
 884 the color bar indicates a density of $>2.5 \times 10^3 \text{ kg m}^{-3}$ and the minimum value is <0.5
 885 $\times 10^3 \text{ kg m}^{-3}$. (e) Density error $\Delta\rho = (\rho_i^{up} - \rho_i^{low})/2$. The maximum value of the color
 886 bar indicates a density error of $>0.25 \times 10^3 \text{ kg m}^{-3}$.

887

888